OPEN ACCESS
Journal of Multidisciplinary Applied Natural Science Vol. 6 No. 2 (2026) https://doi.org/10.47352/jmans.2774-3047.369
Check for updates
Research Article

Correlation of Solar Activity and Interplanetary Parameters on Cosmic rays Intensity Investigated through Multivariate Analysis from 1964 to 2020

Annisa Novia Indra Putri* and Dhani Herdiwijaya

Received : May 8, 2025	Revised : August 28, 2025	Accepted : December 29, 2025	Online : March 10, 2026

Abstract
This study investigated the relationship between the most influential solar and interplanetary plasma parameters and cosmic ray modulation. A principal component analysis (PCA) method was used. The variations of the cosmic ray intensity were obtained at 6 different locations with different latitudes and cutoff rigidities. These stations were located at mid- to high latitudes (SOPO, OULU, and NEWK), while the remaining three were located at low latitudes (MXCO, TSMB, and PSNM). A parameter ranking based on PCA confirmed that sunspot number, interplanetary magnetic field (IMF) magnitude, heliospheric current sheet (HCS) tilt, halo coronal mass ejection (CME) velocity, B_z, and proton density have the highest link with the modulation of cosmic ray intensity. Meanwhile, the PCA analysis at low latitudes revealed that the cone angle and the magnetic field components B_y and B_x along the y - and x-axes, the mean magnetic field of the Sun, the HCS tilt, and the IMF magnitude exert the greatest correlation on the cosmic ray intensity modulation at this station. The correlation between the analyzed parameters and cosmic ray modulation appears to vary with latitude.

Keywords: cosmic ray, interplanetary space, PCA, sun activity

1. INTRODUCTION

Cosmic rays expose charged particles that propagate through interplanetary space and approach the Earth from all directions with high energies. Cosmic ray particles consist of approximately 90% protons, 9% alpha particles, and 1% heavier nuclei [1]. Incoming cosmic rays interact with particles in the Earth's atmosphere, emitting secondary particles such as protons, neutrons, positive–negative pions, and positive–negative kaons. Some of the pion and kaon particles decay into muons and neutrinos.

Galactic cosmic ray particles reach the solar system against the outward sweep of the magnetic field carried by the solar wind, resulting in lower intensity in the solar system. The random motion of cosmic ray particles is a Markov process, as represented by the Fokker-Planck equation [2]. The random motion concept for particle motion has been extended to include the anisotropic case of preferential diffusion along magnetic lines of force. Cosmic ray particles will lose energy as they travel to the Earth. However, direct collisions between reflected cosmic ray particles and the wind field can result in an energy exchange between the wind and galactic cosmic ray particles. This process transfers a significant portion of the solar wind's energy into the cosmic rays that fill interstellar space.

The intensity of galactic cosmic rays on Earth varies over an 11-year cycle, which is anti-correlated with the 11-year cycle of the Sun marked by sunspot number [3]. The anti-correlation also exhibits a time lag [3]-[6] between the peak minima of the cosmic rays and the peak maxima of solar activity or vice versa [7]. The lag between solar activity and cosmic rays exhibits a quasiperiodic characteristic that corresponds to the Sun's magnetic polarity cycle of 22 years [8]. The time lag is also generally attributed to the outward propagation of the solar wind, which carries the heliospheric magnetic field (HMF), and the inward diffusive transport of cosmic ray particles, influenced by large-scale drifts [9]. This phase lag can cause long-term variations in the relationship between cosmic ray intensity and solar activity; distinct time lags for distinct cycles are viewed as

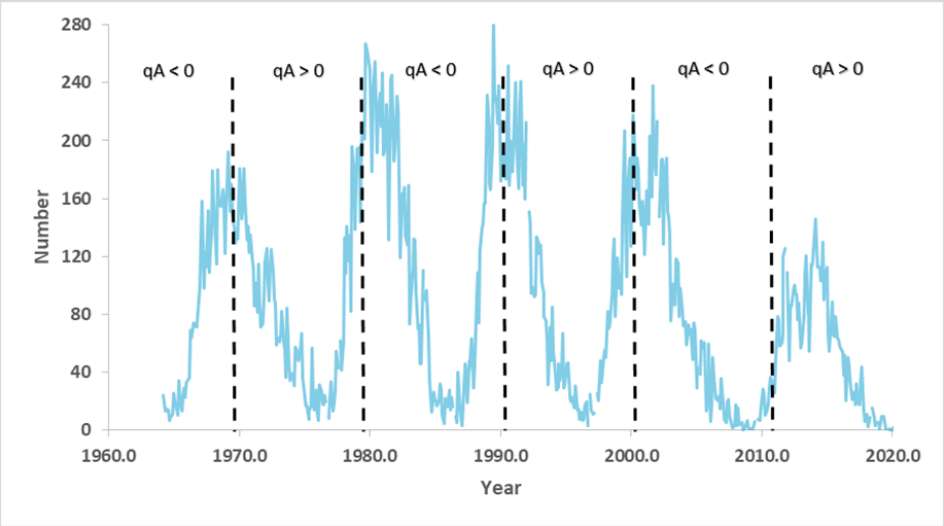

Figure 1. Time series of the raw sunspot number.

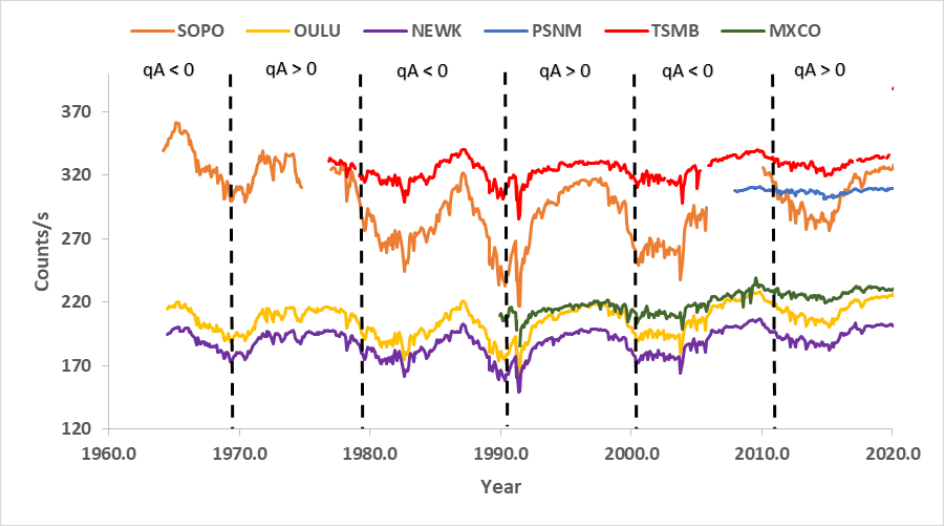

Figure 2. Pressure-corrected neutron monitor counting rates for the summed tubes from the stations of SOPO (orange), OULU (yellow), NEWK (purple), MXCO (green), TSMB (red), and PSNM (blue). The OULU and NEWK count rates have been multiplied by 2, while the PSNM count rate has been divided by 2. The vertical dashed line indicates the approximate epoch of the Sun's mean magnetic field polarity reversal (qA).

the result of large-scale drifts of GCR in the heliosphere.

Sunspots have little direct effect on cosmic-ray intensity, but surface magnetic activity, particularly large and long-lived active patches, can cause disruptions in the characteristics of the solar wind [10], modulating cosmic ray transport in the heliosphere. The journey of cosmic rays to Earth depends on the tilt of the heliospheric current sheet (HCS) from the Sun's equator [11]. When the HCS is tilted and disturbed, the length of the path traveled by the cosmic rays increases, thereby increasing the lag time [12]. The relationship between cosmic ray intensity and HCS tilt angle is anti-correlated with the time-lag difference between the even and odd cycles and between positive and negative polarities. Studying the cosmic ray modulation is essential when considering interplanetary space as a medium of cosmic ray propagation. The transport of cosmic rays in the heliosphere involves drift caused by the magnitude gradient and curvature of the interplanetary magnetic field (IMF) magnitude. Cosmic ray scattering is caused by the non-uniformity of the IMF magnitude [13]. The variation of the time lag between the even and odd cycles of the Sun is

characterized by the reversal of the magnetic polarity of the Sun's poles, which is thought to also account for differences in the peak shape of cosmic ray intensity [14]. The sign of the particle's electric charge is denoted by q, while the polarity of the solar magnetic field is marked by A. The solar magnetic field reverses, causing the north and south magnetic poles to shift positions. The solar magnetic polarity, A, is the large-scale magnetic orientation of the Sun during a specific phase of the cycle. For $A > 0$ indicates the field is outward in the northern hemisphere, while $A < 0$ indicates the field is inward. In this study, we focus on positively charged Galactic cosmic ray particles with $q > 0$. In this context, the sign of the product qA is important because it influences the drift patterns of these particles through the heliosphere. However, it is important to note that the solar cycle itself is defined by the sign of A, independent of the particle type. During $qA > 0$, the IMF's gradient and curvature magnitude allow a drift stream of cosmic rays to reach the heliosphere from the polar regions and be ejected along the equatorial current sheet, and vice versa. During $qA < 0$, the drift stream of cosmic rays reaches the heliosphere through the HCS and exits the polar regions [15]. Research on cosmic ray intensity in the IMF magnitude shows that the IMF magnitude conditions largely control the recovery of cosmic rays [16][17]. During an even cycle, the polarity is $qA < 0$ in the ascending phase and $qA > 0$ in the descending phase, so the cosmic ray recovery is faster after a solar maximum. In contrast, during an odd cycle, the polarity is $qA > 0$ in the ascending phase and $qA < 0$ in the descending phase [18]. The time lag in the $qA < 0$ epoch is greater during the rising phase compared to the falling period of cosmic rays. In the $qA > 0$ epoch, there was only a modest time lag in the descending of cosmic rays [19]. This phenomenon is primarily caused by temporal changes in the structure of IMF magnitude turbulence.

The variability of cosmic-ray intensity is also associated with the solar wind. The interaction of cosmic rays and the solar wind results in energy loss and transfer between them. When solar activity is high, the solar wind is greater, deflecting and slowing cosmic ray particles, reducing their energy. The difference in cosmic ray propagation during the qA period is also dependent on the latitude of the solar wind [20]. Structural changes in solar wind magnetic disturbance during various phases of solar activity are the general mechanics underlying the 11 -year variations in cosmic ray [21]-[24]. The intensity of cosmic rays with the speed of the solar wind is negatively correlated with the time lag over a certain period [25].

Several investigations on cosmic ray modulation on different parameters yield mutually supportive results. The criteria evaluated for cosmic ray modulation must still be minimized in order to focus more on studying and investigating the

Table 1. Cosmic ray intensity monitoring stations according to altitude.

Station	Interval Time	Long. (°)	Lat. (°)	R_c (GV)	Altitude (m)	Detector
OULU	1964–2020	25.5 E	65.1 N	0.81	15	9-NM-64
NEWK	1964–2020	75.8 W	39.7 N	2.40	50	3 x 3-NM-64
TSMB	1977–2020	17.58 E	19.2 S	9.15	1240	Standard 18-NM64
MXCO	1990–2020	99.18 W	19.33 N	8.20	2274	Standard 6-NM-64
PSNM	2008–2020	98.5 E	18.59 N	16.8	2565	Standard 18-NM64
SOPO	1964–2020	0.0 E	90.0 S	0.10	2820	3 x 1-NM-64

Table 2. qA correlation for SOPO, OULU, and NEWK stations.

Station	$qA < 0$	$qA > 0$
SOPO-OULU	0.450	0.806
SOPO-NEWK	0.799	0.844
OULU-NEWK	0.743	0.990

Table 3. Information about the parameters used in this study.

Parameter	Interval Time	Unit	Initial Resolution	Source
Sunspot numbers	1950–2020	Number	Daily	http://sidc.oma.be/silso/datafiles/
Mean magnetic field of the Sun	1975–2020	μT	Daily	http://wso.stanford.edu/
HCS tilt angle	1976–2020	degrees (°)	Carr. Rot.	
Solar wind speed	1963–2020	km s^{-1}	Daily	
Proton density	1963–2020	cm^{-3}	Daily	
IMF magnitude	1963–2020	nT	Daily	
Clock Angle	1963–2020	degrees (°)	Daily	
Cone Angle	1963–2020	degrees (°)	Daily	https://omniweb.gsfc.nasa.gov/
$B_{x,}$ GSM coordinates	1963–2020	nT	Daily	
$B_{y,}$ GSM coordinates	1963–2020	nT	Daily	
$B_{z,}$ GSM coordinates	1963–2020	nT	Daily	
SPEs	1967–2020	1/(cm^2-sec-ster)	Daily	
Halo CME Speed	1996–2020	km s^{-1}	Daily	https://cdaw.gsfc.nasa.gov/
Halo CME Mass	1996–2020	g	Daily	

HCS tilt angle: heliospheric current sheet; IMF: interplanetary magnetic field; B_x, B_y, and B_z; interplanetary magnetic field components; GSM: Geocentric Solar Magnetospheric; SPEs: Solar Proton Events with solar proton flux > 10 MeV.

Figure 4. Effect of gallic acid administration for 8 weeks on serum HDL levels in normal and diabetic

	SOPO	OULU	NEWK	MXCO	TSMB	PSNM
SOPO		0.82	0.85	0.80	0.79	0.76
OULU	0.82		0.99	0.85	0.84	0.82
NEWK	0.85	0.99		0.82	0.83	0.81
MXCO	0.80	0.85	0.82		0.74	0.70
TSMB	0.79	0.84	0.83	0.74		0.49
PSNM	0.76	0.82	0.81	0.70	0.49	

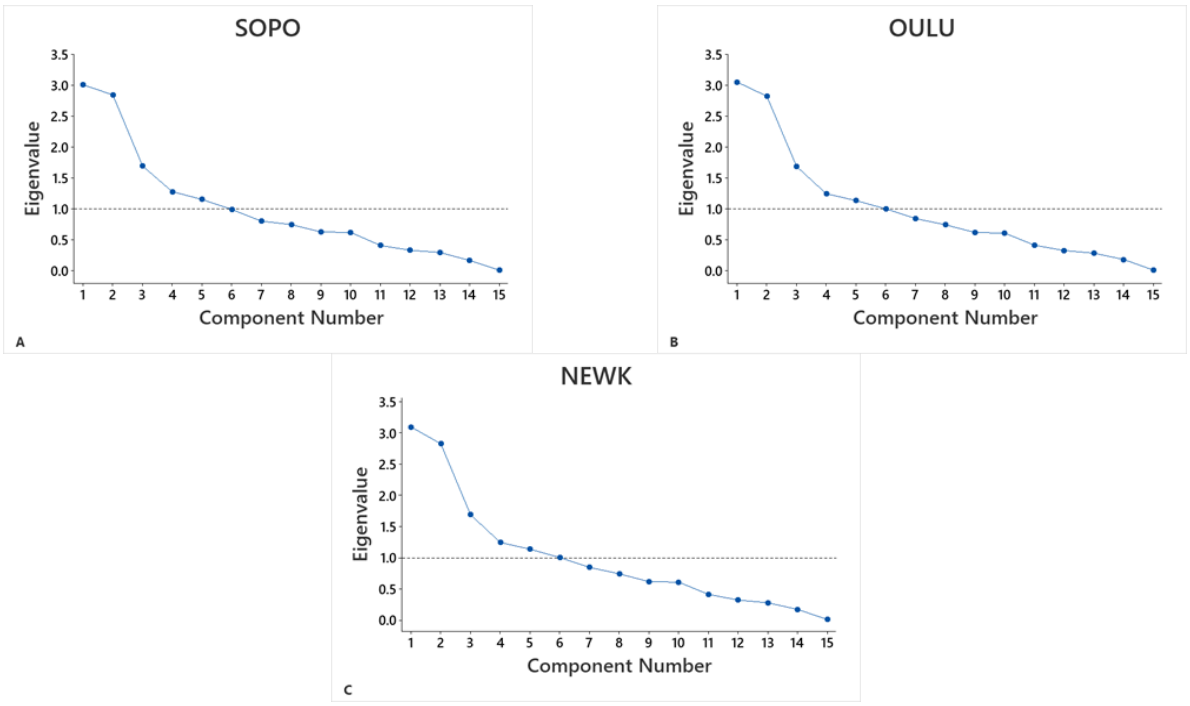

Figure 3. PCA scree plots for the three monitoring stations: (A) SOPO, (B) OULU, and (C) NEWK. The plots show the eigenvalue explained by each principal component, helping to identify the number of components that contribute most significantly to the data structure at each station. The horizontal dotted line indicates eigenvalue = 1.0.

qualities that make the greatest contribution to cosmic ray modulation. The partial least squares (PLS) method approach reveals that the sunspot number, IMF magnitude, and HCS tilt angle parameters are the strongest for higher latitude stations, whereas cone angle, B_x, and B_y are the strongest for lower latitude stations [26]. PLS and PCA approaches have been applied in other non-astrophysics investigations, including biomass gasification [27], flight load calculations [28], and soil qualities [29], to compare results. However, research in astrophysics, particularly solar physics, is limited. The primary goal of this study is to determine the parameters that most strongly correlate with cosmic ray modulation and then examine their impact on cosmic ray modulation using different methodologies to compare recent results.

2. DATA AND METHODS

2.1. Data

Long-term modulation data of cosmic ray intensity observed on Earth were retrieved from the Neutron Monitor Database (NMDB) (http://www01.nmdb.eu/). The pressure- and efficiency-corrected cosmic ray intensity data were obtained at six stations located at different altitudes, latitudes, and cutoff rigidities, namely the South Pole (SOPO) in Antarctica, Oulu (OULU) in Finland, Newark

(NEWK) in America, Mexico City (MXCO) in Mexico, Tsumeb (TSMB) in Namibia, and Princess Sirindhorn Neutron Monitor (PSNM) in Thailand. Data on cosmic ray intensity resolution is also used daily. Figure 1 and Figure 2 shows the sunspot number time series (upper) and pressure- and efficiency-corrected cosmic ray intensity data from six observation stations (lower). The missing line in Figure 2 at the SOPO station is an indication of the absence of data for the years 1974–1976. Table 1 shows information about cosmic ray intensity data, where R_c is the geomagentic cutoff rigidity of each station. The cosmic ray research regularly uses rigidity to examine geomagnetic field shielding. Thus, the geomagnetic field shielding effect can be quantified as the geomagnetic cutoff rigidity [30]. When the time is fixed, at a particular location and incidence angle, the geomagnetic cutoff rigidity R_c acts as a limit value, and only particles with value greater than this limit value can enter the Earth's atmosphere [31].

We tested the correlation between SOPO-OULU, SOPO-NEWK, and OULU-NEWK for each *qA* cycle ($qA < 0$ and $qA > 0$). SOPO-OULU has the farthest hemisphere distance, while OULU-NEWK has the closest hemisphere distance. The correlation results can be found in Table 2. It demonstrates that SOPO-OULU has the lowest correlation value at $qA < 0$ and OULU-NEWK has the maximum correlation value at $qA > 0$. Furthermore, correlation values at $qA > 0$ are significantly larger than those at $qA < 0$. During the $qA < 0$, the solar flux component of the approaching field vector is bigger than that of the away field vector. However, no asymmetry between the solar magnetic field north and south of the HCS was detected in the $qA > 0$ epoch [32].

In this paper, the cosmic ray modulation will be analyzed against sunspot number, IMF magnitude, HCS tilt angle, mean magnetic field of the Sun, and solar wind speed. The HCS tilt angle model employs radial boundary conditions at the photosphere, yielding results computed with a greater source surface radius (3.25 $R_{\odot}$). The IMF magnitude parameters are the clock angle θ and cone angle ϕ. The clock angle is defined as the direction of the IMF magnitude in the y–z plane of the geocentric solar magnetospheric (GSM) coordinate system [33], whereas the cone angle is the angle formed between the IMF magnitude direction and the Earth-to-Sun line [34]. These two parameters are calculated by Equations 1 and 2, where B is the IMF magnitude, and B_x, B_y, and B_z are its components in the x, y, and z directions, respectively:

$$\theta = \arctan \frac{-B_y}{Bz} \quad \textbf{(1)}$$

$$\varphi = \arccos \frac{-B_x}{B} \quad \textbf{(2)}$$

Meanwhile, the solar wind parameters are proton density and plasma velocity. The observation periods and sources of these 11 parameters are listed in Table 3, with the data resolution ranging.

Coronal mass ejection (CME) is a crucial energetic solar activity that dominates circumstances in interplanetary space and has an effect on Earth [35]. Spacecraft will identify CMEs

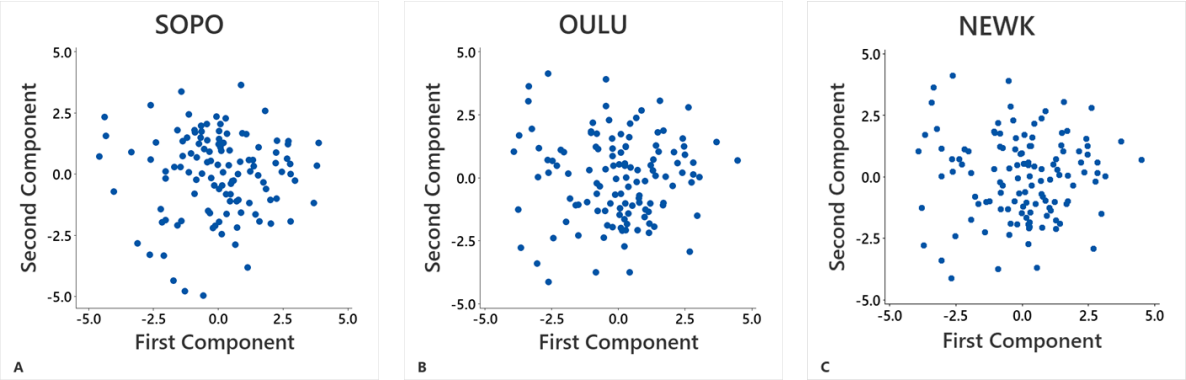

Figure 4. PCA score plots for the three stations: (A) SOPO, (B) OULU, and (C) NEWK. The plots display the distribution of samples based on the first two principal components, reflecting similarities and differences in the data structure across the monitoring sites.

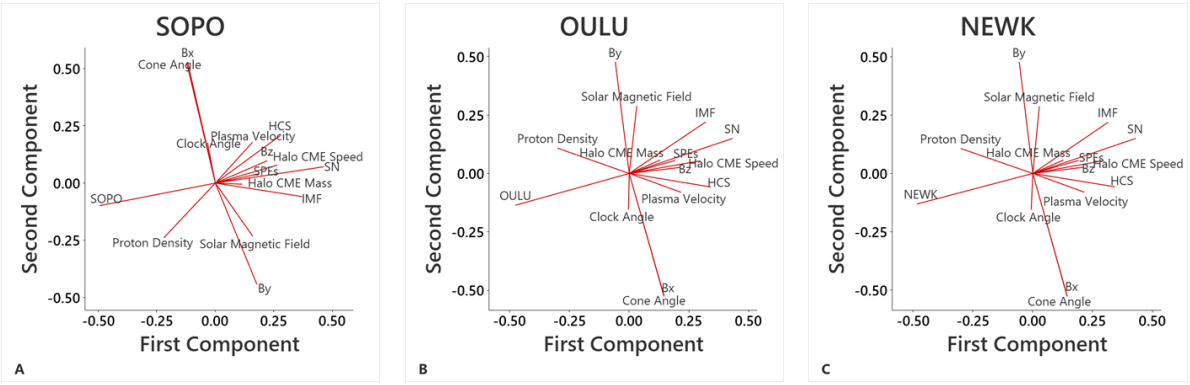

Figure 5. PCA loading plots for (A) SOPO, (B) OULU, and (C) NEWK stations. The plots illustrate the contribution of each variable to the first two principal components, highlighting the dominant patterns of variability at each site.

Table 5. First two PCA components of data from the SOPO, OULU, and NEWK stations.

Parameter	SOPO		OULU		NEWK	
	PC1	PC2	PC1	PC2	PC1	PC2
Sunspot number	0.463	0.071	0.432	0.150	0.429	0.150
IMF magnitude	0.370	−0.059	0.319	0.220	0.315	0.219
HCS tilt angle	0.277	0.207	0.341	−0.058	0.341	−0.057
Halo CME speed	0.264	0.079	0.296	0.054	0.296	0.055
B_z	0.222	0.098	0.212	0.026	0.211	0.026
SPEs	0.188	0.041	0.192	0.056	0.191	0.056
B_y	0.177	−0.442	−0.058	0.477	−0.057	0.477
Mean magnetic field of the Sun	0.160	−0.232	0.032	0.288	0.027	0.287
Plasma velocity	0.159	0.179	0.216	−0.080	0.215	−0.080
Halo CME mass	0.114	−0.005	0.130	0.057	0.128	0.058
Clock angle	−0.034	0.176	−0.003	−0.154	−0.007	−0.155
B_x	−0.119	0.529	0.146	−0.525	0.144	−0.526
Cone angle	−0.122	0.522	0.144	−0.520	0.142	−0.520
Proton density	−0.220	−0.239	−0.299	0.108	−0.300	0.106

SOPO (PC1: -0.494; PC2: -0.098); OULU (PC1: -0.476; PC2: -0.136); NEWK (PC1: -0.484; PC2: -0.131)

that have reached interplanetary space as interplanetary coronal mass ejections (ICMEs). ICME also can block cosmic-ray particles [36][37]. Therefore, the ICME parameters become essential in analyzing the modulation of cosmic rays arriving at Earth. In this paper, we use the CME halo parameters such as linear speed and ejected mass. Halo CME data was not a continuous time series, but rather discrete data collected just during the CME halo event. CME occurrences are frequently accompanied by other types of plasma activity, such as bursts of energetic protons into interplanetary space. These energetic proton bursts are called solar proton events (SPEs). As a result, we take into account the SPE flux data type for proton fluxes greater than 10 MeV as another parameter.

2.2. Methods

To predict the correlation between the response (cosmic ray modulation) and several predictors, we applied PCA with code from Minitab software. PCA is a dimensionality reduction method for large data. It works by reducing a large collection of variables into a smaller one that retains the majority of the information from the larger set. PCA is an analytical method that explains linear multivariate

models on complex data [38]. This multivariate data reduction technique identifies the correlations between variables [39][40] using orthogonal basis vectors or principal components (PCs). As samples with nearly identical PCs have very similar characteristics, PCA is also used for grouping. PCs are ordered by variance from largest to smallest, so the first PC is expected to have more significant variation in the data than subsequent PCs [41]. Most of the variability tends to be captured by the first PC, while the last PC contains little information from the original variables.

There are three steps of the PCA method: First, make standardization. Standardization is important before PCA since the latter is particularly sensitive to differences in the original variables. Thus, converting the data to equivalent scales can avoid this issue. This can be accomplished mathematically by subtracting the mean from each variable's value and dividing by the standard deviation. Second, computing the correlation or covariance matrix. The purpose of this stage is to understand how the variables in the input data set depart from the mean in respect to one another or to identify whether there is a relationship between them. Because variables might become strongly connected to the point of containing redundant information. Third, computing the eigenvectors and eigenvalues. A PCA seeks a set of orthogonal eigenvectors from the correlation or covariance matrix variables. The independent variable matrix and the eigenvector matrix combine to form the PC matrix. The eigenvectors contain the weight coefficients corresponding to each variable from which the PC score is calculated. The eigenvectors are obtained as columns of orthogonal matrices during the spectral decomposition of the covariance or correlation matrices (S or R, respectively). This research adopts the correlation matrix. As the matrix R is symmetric, the orthogonal matrix V can be written as follows by Equations 3 and 4.

$$V'RV = D \quad \textbf{(3)}$$

$$R = VDV \quad \textbf{(4)}$$

where D is a diagonal matrix in which the diagonal elements are eigenvalues, and the columns of V are eigenvectors. PCA methods output a score, which is a linear combination of the original variables explaining the variance in the data. The PC scores are collected into an $n \times m$ matrix Z determined as Z = YV, where Y is a standardized data matrix ($n \times p$) used by the correlation matrix method and V is the eigenvector matrix ($p \times m$). By ordering eigenvectors in order of eigenvalue, from highest to lowest, it can obtain the principal components in order of significance. PCA is widely applied in chemistry, pharmacy, accounting, and astronomy. In astronomical research, PCA has been applied to physical structural investigation of the interstellar medium [42], galaxy classification [43], quasar stellar objects (QSO) classification [44], studies of Forbush decrease [45], and application to sunspot number [46].

We also attempted a linear multiple regression fitting using multiple linear regression. Multiple linear regression is a statistical technique for

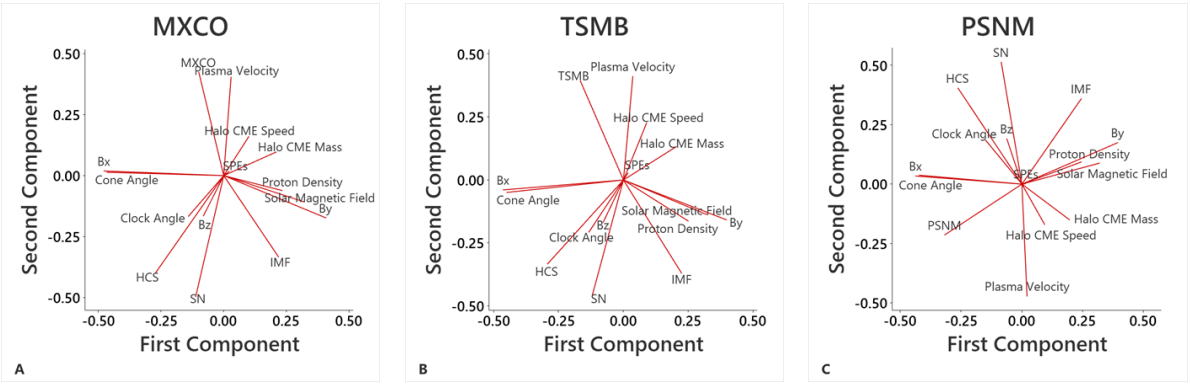

Figure 6. PCA loading plots for (A) MXCO, (B) TSMB, and (C) PSNM stations. The plots illustrate the contribution of each variable to the first two principal components, highlighting the dominant patterns of variability at each site.

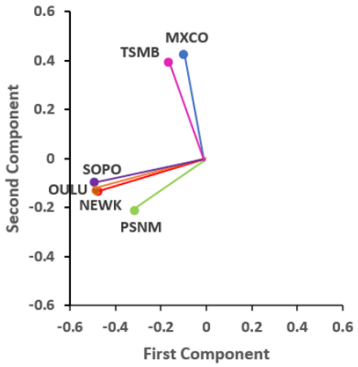

Figure 7. PCA loading plots for six stations using all parameter.

Table 6. First two PCA components of data from the MXCO, TSMB, and PSNM stations.

Parameter	MXCO		TSMB		PSNM	
	PC1	PC2	PC1	PC2	PC1	PC2
B_y	0.408	−0.174	0.398	−0.158	0.394	0.175
Mean magnetic field of the Sun	0.322	−0.108	0.324	−0.138	0.319	0.088
Proton Density	0.234	−0.062	0.251	−0.163	0.245	0.094
IMF magnitude	0.219	−0.334	0.225	−0.371	0.245	0.360
Halo CME Mass	0.210	0.097	0.205	0.133	0.196	−0.151
Halo CME Speed	0.101	0.161	0.090	0.227	0.094	−0.171
Plasma Velocity	0.029	0.404	0.036	0.412	0.021	−0.472
SPEs	0.023	0.018	0.018	0.029	0.016	0.001
B_z	−0.081	−0.166	−0.078	−0.168	−0.062	0.192
Sunspot number	−0.112	−0.497	−0.167	−0.458	−0.085	0.514
Clock Angle	−0.142	−0.168	−0.134	−0.208	−0.149	0.185
HCS tilt angle	−0.273	−0.400	−0.294	−0.334	−0.263	0.405
Cone Angle	−0.467	0.014	−0.451	−0.049	−0.423	0.038
B_x	−0.479	0.019	−0.465	−0.039	−0.438	0.034

MXCO (PC1: -0.100; PC2: 0.424); TSMB (PC1: -0.167; PC2: 0.394); PSNM (PC1: -0.318; PC2: -0.214)

modeling the relationship between a single dependent variable (response) and two or more independent variables (predictors). It is used to determine how well the observation data matches the model created by Equation 5.

$$y = C + a_1x_1 + a_2x_2 + a_3x_3 + \ldots \quad \textbf{(5)}$$

3. RESULTS AND DISCUSSIONS

For the first analysis, we considered three stations—SOPO, OULU, and NEWK—located at high-mid latitudes. Three stations, MXCO, TSMB, and PSNM, located at lower latitudes, will be used to cross-check this study. Table 4 shows the correlation between each station from 1964 to 2020, which conforms to Table 1. Table 4 shows the correlation between high- and low-latitude stations. High correlation indicates that both stations have the same response. The highest correlation value (0.99) is shown by the OULU-NEWK station, while the lowest (0.49) correlation value is shown by the TSMB-PSNM station.

3.1. Eigenvalues and Scree Plots

The eigenvalues (or characteristic values) are the variances of the PCs used for determining the number of PCs. The present study assumes Kaiser's

criteria, under which PCs with an eigenvalue greater than or equal to one are maintained. In PCA, the selected PCs are predicted to explain the most variance in the data, and the variance explained by the PCs is determined using the eigenvalues. The eigenvalues show how much variance is explained by each PC. A PC with an eigenvalue > 1 explains at least as much variance as one original variable; vice versa, components having an eigenvalue less than one are deemed insufficiently informative because they explain no more variation than a single original variable. The Kaiser criterion simplifies identifying the number of components to maintain, eliminating the need for sophisticated analysis or searching for eigenvalues less than 1. The restriction on eigenvalues ≥ 1 makes this criterion straightforward to apply in a number of contexts, including large and small data analysis.

A scree plot is used to identify statistically significant factors or components, which is often referred to as a test [47]. The scree plot displays the eigenvalues as a function of PC number, where the eigenvalues are sorted from largest to smallest. The eigenvalues of the correlation matrix are the variances of the PCs. From the scree plot, we can select the number of components for the analysis. Ideally, the scree plot shows an initial steep decline followed by a bend and a linear decrease. The PCs on the steep part of the curve (before the first point of the straight line) are selected for analysis. The scree plots of the data at the three stations are shown in Figure 3. As the eigenvalues in all plots follow a linear decline after the fifth PC, the first five PCs were maintained for further analysis.

3.2. Score Plots

The score plot is a graph of the second PC's score against the first PC's score. When examining

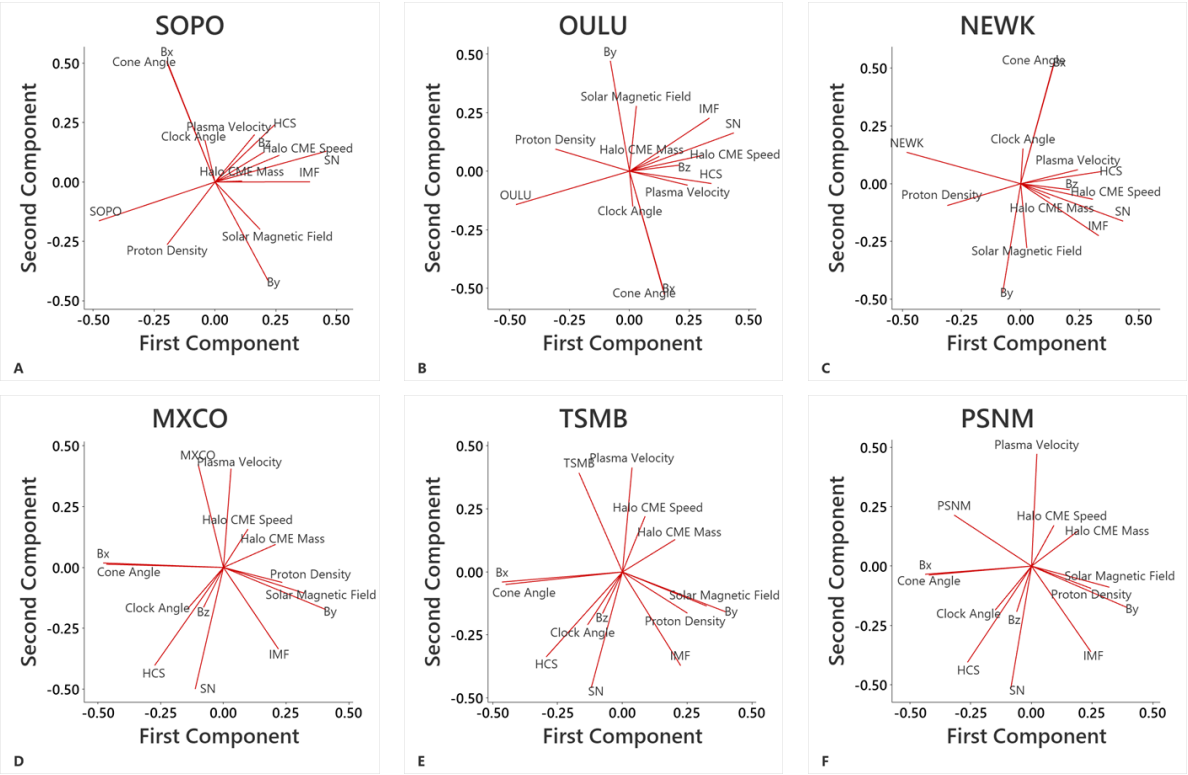

Figure 8. PCA loading plots for (A) SOPO, (B) OULU, (C) NEWK, (D) MXCO, (E) TSMB, and (F) PSNM stations without SPEs. The plots illustrate the contribution of each variable to the first two principal components, highlighting the dominant patterns of variability.

Table 7. The standard deviation and average for the difference between the model and data.

	SOPO	OULU	NEWK	MXCO	TSMB	PSNM
Standard Deviation	4.103	2.584	2.319	1.747	9.521	0.421
Average	−0.678	−0.431	−0.481	1.748	−1.008	−0.019

Table 8. Best-fit coefficient from the all stations with the first six largest absolute PC1.

Station	C	Sunspot Number	IMF Magnitude	HCS tilt angle	Halo CME Speed	Proton Density	B_z	R^2 (%)
SOPO	344.10 ± 9.61	−0.182 ± 0.031	−4.770 ± 1.36	−0.153 ± 0.067	−0.009 ± 0.003	0.860 ± 1.000	1.980 ± 2.44	59.11
OULU	116.49 ± 2.12	−0.037 ± 0.007	−1.317 ± 0.315	−0.031 ± 0.015	−0.002 ± 0.001	0.255 ± 0.234	0.547 ± 0.573	58.80
NEWK	104.81 ± 1.74	−0.031 ± 0.006	−1.080 ± 0.258	−0.029 ± 0.013	−0.002 ± 0.001	0.269 ± 0.191	0.347 ± 0.469	61.59
Station	**C**	**B_x**	**Cone Angle**	**B_y**	**Mean magnetic field of the Sun**	**HCS tilt angle**	**IMF Magnitude**	**R^2 (%)**
MXCO	230.0 ± 17.5	−2.40 ± 1.91	0.189 ± 0.192	−1.167 ± 0.651	0.040 ± 0.034	0.003 ± 0.012	−4.600 ± 0.273	56.48
TSMB	348.8 ± 14.0	0.11 ± 1.46	0.033 ± 0.153	0.706 ± 0.496	0.081 ± 0.027	−0.134 ± 0.015	−3.578 ± 0.216	58.26
PSNM	657.6 ± 17.3	3.87 ± 2.25	−0.348 ± 0.190	−1.274 ± 0.692	−0.102 ± 0.037	−0.043 ± 0.015	−1.974 ± 0.389	50.99

this plot, look for the leverage points and clusters. The score plot in the PCA method is used for assessing data structures and detecting clusters, outliers, and data trends. If the data follows a normal distribution with no outliers, then the data points are randomly distributed around zero. Figure 4 shows that no data points are classed as leverage points or clusters. Aside from that, the data points are evenly distributed with no obvious outliers. The data can be appropriately represented by a normal distribution.

3.3. Loading Plots

The loading plot depicts the coefficients of each variable in the second component versus those of the first component. From a loading plot, we can identify the variables that most significantly correlate with each component and characterize the variables in each component. The loading plots obtained by the PCA are given in Figure 5. Specifically, the first component (PC1) appears to represent a dominant temporal variation associated with solar modulation effects, while the second component (PC2) likely reflects sectorial structures in the interplanetary magnetic field. These interpretations are supported by the loading patterns and the temporal/spatial behavior observed in the projections. The absolute value of PC1 is mainly contributed by cosmic ray intensity, sunspot number, IMF magnitude, and HCS tilt angle, as indicated by the longer vector lines of these parameters than for the other parameters. This result is supported by the qualitative results in Table 5, which show the highest PC1 values for sunspot number, IMF magnitude, and HCS tilt angle. Meanwhile, the absolute value of the PC2 is dominated by the cone angle, B_x, and B_y parameters.

The vector directions in the loading plots differ between the SOPO and OULU/NEWK stations. These differences are found for clock angle, cone angle, plasma velocity, proton density, mean magnetic field of the Sun, B_x, and B_y. The vectors of the cosmic ray parameters (sunspot number, IMF magnitude, HCS tilt angle, B_z, halo CME speed, halo CME mass, and SPEs) show the same directions in all plots. The parameters having the same vector direction at the three stations are in the same position relative to the cosmic ray intensity,

with an angle of nearly 180°, indicating that they negatively correlate with cosmic ray intensity. Meanwhile, the parameters with different vector directions at the three stations form an angle close to 90° with respect to the cosmic rays, meaning that they are almost uncorrelated with cosmic ray intensity. Sunspot number, IMF magnitude, plasma velocity, HCS tilt angle, B_z, halo CME speed, halo CME mass, and SPEs could be grouped together, indicating that these parameters have similar internal characteristics. Although the plasma velocity shows a different vector direction in Figure 5, its vector position appears to be included in the sunspot number group, which is negatively correlated with cosmic ray intensity.

3.4. Latitude and Cutoff Rigidity Function

Solar activity, measured by the worldwide sunspot number, impacts the heliosphere. The environment's shifts impact cosmic ray propagation in the heliosphere, which causes a time lag. The modulation lag reduces with cosmic particle rigidity and energy. In this paper, the latitude and R_c were tested at lower latitudes to observe the characteristics of the parameters utilized. The observation sites were Mexico City (MXCO) in Mexico, Tsumeb (TSMB) in Namibia, and Princess Sirindhorn Neutron Monitor (PSNM) in Thailand, which were compared during the same period (2007 -2020). The results of the first two principal components (PC1 and PC2) and loading plots at the three stations are described in Table 6 and Figure 6.

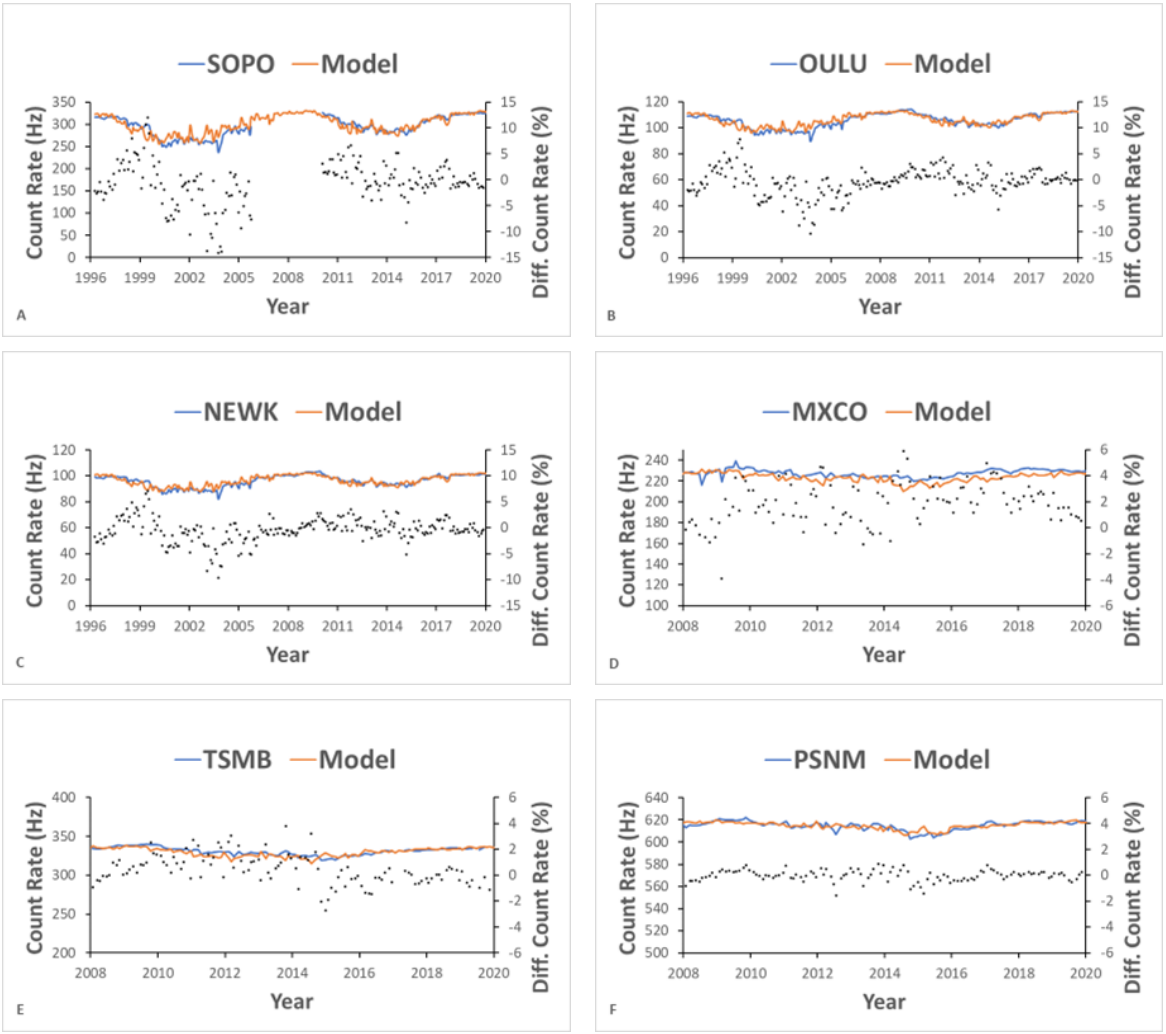

Figure 9. Comparison of counting rates from the stations: (A) SOPO, (B) OULU, (C) NEWK, (D) MXCO, (E) TSMB, and (F) PSNM. The observed counting rates (blue line) and the corresponding model predictions (orange line) are plotted over time using the left vertical axis. The percentage differences between the observed values and model predictions are represented by black dots, plotted using the right vertical axis.

In Figure 6, the parameters at the PSNM station have different vector directions from MXCO and TSMB, but all three stations show the same PC1 sequence. The top three parameters, B_x, cone angle, and B_y, gave the highest absolute PC1 values for all three stations. These results differ from those of the three previous stations, implying that at lower latitudes, the strength parameter depends on the angle of the magnetic field. As the cone angle is a function of Bx, these two parameters undergo similar physical processes. Figure 7 also displays the findings between PC1 and PC2 for the six stations used. This graphic shows three clusters: the MXCO-TSMB cluster, the SOPO-OULU-NEWK cluster, and the PSNM cluster.

3.5. The Role of CME Phenomenon

CMEs are energetic events caused by solar activity that have a significant impact on interplanetary space conditions. The CME phenomena can even keep cosmic rays from hitting the heliosphere's interior [48][49]. The latitude of a CME correlates with the modulation of cosmic rays. The latitude of a CME refers to the geographical or spatial position of the related active region. High-latitude CMEs exhibit a stronger association with cosmic ray modulation than low-latitude CMEs. This suggests that high-latitude CMEs have a greater impact on cosmic ray intensity [50]. Strong CMEs generate shocks powerful enough on their flanks to induce considerable cosmic ray drops for observers who detect the shocks outside the azimuthal reach of the 'driver' CMEs [51]. This phenomenon, called the Forbush decrease, is a short -term decrease in cosmic ray intensity that often occurs after a CME. As a result, CME is an important metric in investigating cosmic ray modulation. As a comparison, all high- and low-latitude cosmic ray stations are included in the study in this section. Figure 8 depicts the loading plot results for all cosmic ray observation stations calculated using the PCA approach without the SPEs parameters. The loading plot graphs for SOPO, OULU, MXCO, and TSMB stations are the same as in Figures 5 and 6. Figure 8 also depicts vector changes at the NEWK and PSNM stations. The NEWK station shows vector direction changes in the cone angle, clock angle, B_x, B_y, and mean magnetic field of the Sun parameters, while the PSNM station shows the same loading plot graph as the MXCO and TSMB stations. Despite changes in vector direction, the PC1 order for all stations is the same as the results in Tables 5 and 6.

3.6. Multiple Linear Regression

We analyze the first six parameters with the highest absolute PC1, namely the sunspot number, IMF magnitude, HCS tilt angle, halo CME speed, proton density, and B_z for SOPO, OULU, and NEWK stations, and the B_x, cone angle, B_y, mean magnetic field of the Sun, HCS tilt angle, and IMF magnitude for MXCO, TSMB, and PSNM stations. PC1 is the first principal component generated by PCA, and it represents the direction with the most variance in the data. PC1's values are the first linear combination that captures the most variation, while PC2 (the second principal component) captures the next largest variation, and so on. Considering that B_x, B_y, and the cone angle are all derivative parameters of the IMF magnitude, it is reasonable to suppose that the IMF magnitude component is also important at lower latitude stations. Figure 9 depicts a graph of the data (blue line), models (orange line), and their differences (black dots). The difference in count rate between the data and the model can reveal period changes. The graph also depicts two distinct trajectories for SOPO, OULU, and NEWK stations. Before 2005, the discrepancies are greater, whereas after 2005, they are lower. This is because there are a number of data gaps on the halo CME speed parameter after 2005. This figure also shows that the deviations from zero (on the right scale) are most significant in the order of MXCO, TSMB, and PSNM.

Table 7 shows the standard deviation and average values for the black dots in Figure 9. The PSNM displays the least standard deviation, whereas the TSMB displays the largest. Table 8 displays the results of various linear regression fits using ordinary least squares. The R^2 values for the first six stations are around 50–60%.

3.7. Discussions

We examined the correlation of several solar activity and interplanetary space plasma parameters on cosmic ray modulation. The initial analysis data were acquired from three stations (SOPO, OULU, and NEWK) that are on the high-mid latitudes and

had varied R_c values. We considered 14 parameters: sunspot number, IMF magnitude, clock angle, cone angle, proton density, plasma velocity, mean magnetic field of the Sun, HCS tilt angle, B_x, B_y, B_z, halo CME speed, halo CME mass, and SPEs.

The data of the three stations were similarly grouped in the loading plots, indicating they have the same similar physical processes. We presumed that these parameters, especially the sunspot number (0.44), IMF magnitude (0.33), and HCS tilt angle (0.31), play an essential role based on PC1 order at high-middle stations [52]. The IMF magnitude configuration leads to small-scale changes in its direction and magnitude, expansion of the magnetic field structure, shock waves, and tangential discontinuities [53]. For these reasons, the IMF magnitude parameters generate both short-term and long-term cosmic ray modulation effects. The HCS tilt angle also produces a radial and latitudinal shift. When the HCS tilt angle is high, cosmic rays can pass through the inner heliosphere [54]. Moreover, the CME phenomenon links high solar activity to non-recurring geomagnetic storms. The initial velocity of the CME relative to the surrounding solar wind largely determines whether a coronal mass ejection directed at Earth will be geomagnetically effective or ineffective [55].

At lower latitudes, we discovered that the most important parameters for cosmic ray modulation are B_x (0.46), cone angle (0.45), and B_y (0.4), which represent the magnetic components and orientation of the interplanetary magnetic field. This discrepancy indicates a separate physical mechanism, particularly at low latitudes around the equator. Cosmic-ray modulation at high R_c is caused by a high diffusion coefficient due to changes in magnetic field strength along the heliosphere [56]. Diffusion coefficients determine access to the inner heliosphere, with higher values resulting in shorter pathways along long and slanted current sheets [57]. Cosmic rays flowing through the heliosphere with high R_c and significant diffusion coefficients result in diverse solar modulation patterns.

We also include the best five parameters for fitting the model to the data using a multiple linear regression technique. The difference between the model and the TSMB station data generates the highest R^2 score. Furthermore, the PSNM station is not in the same cluster as MXCO-TSMB on the loading plot, despite the fact that all three are in the low station category. This is believed to be related to the MXCO-TSMB station's proximity to the South Atlantic Anomaly region (SAA), which influences the distribution of cosmic rays [58]. The PAMELA experiment observed substantially higher quantities of antiprotons than expected as it passed through the SAA. This suggests that the Van Allen belts include antiparticles created by the interaction of the Earth's upper atmosphere with cosmic rays [59].

4. CONCLUSIONS

We compared cosmic ray intensities at six stations with varying latitudes and R_c values (SOPO, OULU, NEWK, MXCO, TSMB, and PSNM) to 14 parameters of solar activity and interplanetary plasma space. First, we employ three stations, SOPO, OULU, and NEWK, which are classified as high- to mid-latitude. We demonstrate via PCA that the sunspot number, IMF magnitude, HCS tilt angle, and halo CME speed have the strongest correlations with cosmic ray modulation. The results' comparison to low-latitude stations such as MXCO, TSMB, and PSNM. In contrast, in stations with low latitude and high R_c, cosmic ray modulation is most closely related to B_x, cone angle, and B_y. This variation may be due to differences in the physical processes of cosmic rays received at different latitudes, particularly between high-medium and low latitudes. Using multiple linear regression, the top six parameters showed differences of less than 10% between data and model at high, middle, and low latitudes.

AUTHOR INFORMATION

Corresponding Author

Annisa Novia Indra Putri — Atmospheric and Planetary Sciences Study Program, Institut Teknologi Sumatera, South Lampung-35365 (Indonesia);

orcid.org/0009-0001-6772-8130

Email: annisa.putri@sap.itera.ac.id

Author

Dhani Herdiwijaya — Astronomy Division,

Institut Teknologi Bandung, Bandung-40132 (Indonesia); Bosscha Observatory, Institut Teknologi Bandung, Bandung-40132 (Indonesia); Center for Space Science, Technology, and Innovation, Institut Teknologi Bandung, Bandung-40132 (Indonesia); University Center of Excellence for Space Science, Technology and Innovation, Institut Teknologi Bandung, Bandung-40132 (Indonesia) ;
orcid.org/0000-0001-6630-8735

Author Contributions

Conceptualization, Validation, Investigation, Visualization, and Project Administration, A. N. I. P. and D. H.; Methodology, Supervision, and Writing – Review & Editing, D. H.; Software, Formal Analysis, Resources, Data Curation, and Writing – Original Draft Preparation, A. N. I. P.; Visualization, and Project Administration, A. N. I. P. and D. H.

Conflicts of Interest

The authors declare no conflict of interest.

ACKNOWLEDGEMENT

Dhani Herdiwijaya thanks to Research, Community Service, and Innovation Fund year 2024 and 2025 [616AP/IT1.C02/KU/2024 dan 1K/IT1.C02/KU/2025] from Faculty of Mathematics and Natural Sciences, ITB.

DECLARATION OF GENERATIVE AI

Not applicable.

REFERENCES

[1] T. Dunai. (2010). "Cosmogenic Nuclides: Principles, Concepts and Applications in Earth Surface Sciences". Cambridge University Press, Cambridge. 1-24. 10.1017/CBO9780511804519.

[2] E. N. Parker. (1965). "The Passage of Energetic Charged Particles Through Interplanetary Space". *Planetary and Space Science.* **13** : 9-49. 10.1016/0032-0633(65)90131-5.

[3] S. E. Forbush. (1958). "Cosmic Ray Intensity Variations During Two Solar Cycles". *Journal of Geophysical Research.* **63** : 651-669. 10.1029/JZ063i004p00651.

[4] I. G. Usoskin, H. Kananen, K. Mursula, P. Tanskanen, and G. A. Kovaltsov. (1998). "Correlative Study of Solar Activity and Cosmic Ray Intensity". *Journal of Geophysical Research: Space Physics.* **103** : 9567-9574. 10.1029/97JA03782.

[5] J. A. Van Allen. (2000). "On the Modulation of Galactic Cosmic Ray Intensity During Solar Activity Cycles 19, 20, 21, 22, and Early 23". *Geophysical Research Letters.* **27** : 2453-2456. 10.1029/2000GL003792.

[6] E. Ross and W. J. Chaplin. (2019). "The Behaviour of Galactic Cosmic Ray Intensity During Solar Activity Cycle 24". *Solar Physics.* **294** : 8. 10.1007/s11207-019-1397-7.

[7] B. Bertucci, E. Fiandrini, B. Khiali, and N. Tomassetti. (2019). "Time Lag in Cosmic Ray Modulation and Global Properties of the Solar Cycle". *Proceedings of the 36th International Cosmic Ray Conference*. 6933-6940.

[8] M. Potgieter. (2013). "Solar Modulation of Cosmic Rays". *Living Reviews in Solar Physics.* **10** : 3. 10.12942/lrsp-2013-3.

[9] S. A. Koldobsky, R. Kähkönen, B. Hofer, N. A. Krivova, G. A. Kovaltsov, and I. G. Usoskin. (2022). "Time Lag Between Cosmic -Ray and Solar Variability: Sunspot Numbers and Open Solar Magnetic Flux". *Solar Physics.* **297** : 38. 10.1007/s11207-022-01970-1.

[10] D. Stansby, L. Green, L. van Driel-Gesztelyi, and T. Horbury. (2021). "Active Region Contributions to the Solar Wind Over Multiple Solar Cycles". *Solar Physics.* **296** : 116. 10.1007/s11207-021-01861-x.

[11] M. S. Badruddin and Y. P. Singh. (2007). "Modulation Loops, Time Lag and Relationship Between Cosmic Ray Intensity and Tilt of the Heliospheric Current Sheet". *Astronomy and Astrophysics.* **466** : 697-704. 10.1051/0004-6361:20066549.

[12] O. P. M. Aslam and Badruddin. (2015). "Study of Cosmic Ray Modulation During

Recent Unusual Minimum and Mini-Maximum of Solar Cycle 24". *Solar Physics.* **290** : 2333-2353. 10.1007/s11207-015-0753-5.

[13] P. Morrison. (1956). "Solar Origin of Cosmic Ray Time Variations". *Physical Review.* **101** : 1397-1404. 10.1103/PhysRev.101.1397.

[14] O. P. M. Aslam and Badruddin. (2012). "Solar Modulation of Cosmic Rays During the Declining and Minimum Phases of Solar Cycle 23: Comparison with Past Three Solar Cycles". *Solar Physics.* **279** : 269-288. 10.1007/s11207-012-9970-3.

[15] J. R. Jokipii and B. Thomas. (1981). "Effects of Drift on the Transport of Cosmic Rays IV: Modulation by a Wavy Interplanetary Current Sheet". *The Astrophysical Journal.* **243** : 1115-1122. 10.1086/158675.

[16] P. C. Hedgecock. (1975). "Measurements of IMF in Relation to the Modulation of Cosmic Rays". *Solar Physics.* **42** : 497-527. 10.1007/BF00149929.

[17] H. S. Ahluwalia. (2002). "IMF Intensity and Galactic Cosmic Ray Modulation". *Advances in Space Research.* **29** : 439-444. 10.1016/S0273-1177(01)00609-3.

[18] F. Inceoglu, M. F. Knudsen, C. Karoff, and J. Olsen. (2014). "Modeling the Relationship Between Neutron Counting Rates and Sunspot Numbers Using the Hysteresis Effect". *Solar Physics.* **289** : 1387-1402. 10.1007/s11207-013-0391-8.

[19] K. Iskra, M. Siluszyk, M. Alania, and W. Wozniak. (2019). "Experimental Investigation of the Delay Time in Galactic Cosmic Ray Flux in Different Epochs of Solar Magnetic Cycles (1959–2014)". *Solar Physics.* **294** : 115. 10.1007/s11207-019-1509-4.

[20] N. Tomassetti, B. Bertucci, and E. Fiandrini. (2022). "Temporal Evolution and Rigidity Dependence of the Solar Modulation Lag of Galactic Cosmic Rays". *Physical Review D.* **106** : 103022. 10.1103/PhysRevD.106.103022.

[21] M. V. Alania, R. G. Aslamazashvili, T. B. Bochorishvili, K. Iskra, and M. Siluszyk. (2001). "The Role of Drift on the Diurnal Anisotropy and on Temporal Changes in the Energy Spectra of the 11-Year Variation for Galactic Cosmic Rays". *Advances in Space Research.* **27** : 613-618. 10.1016/S0273-1177(01)00092-8.

[22] M. Siluszyk, K. Iskra, R. Modzelewska, and M. V. Alania. (2005). "Features of the 11-Year Variation of Galactic Cosmic Rays in Different Periods of Solar Magnetic Cycles". *Advances in Space Research.* **35** : 677-681. 10.1016/j.asr.2005.02.037.

[23] K. Iskra, M. Siluszyk, and M. V. Alania. (2015). "Rigidity Spectrum of the Long-Period Variations of the Galactic Cosmic Ray Intensity in Different Epochs of Solar Activity". *Journal of Physics: Conference Series*. **632** : 012079. 10.1088/1742-6596/632/1/012079

[24] M. Siluszyk, K. Iskra, M. V. Alania, and S. Miernicky. (2015). "Feature of the Interplanetary Magnetic Field Turbulences in Different Periods of Solar Magnetic Cycles". *Proceedings of the 34th International Cosmic Ray Conference*. 10.22323/1.236.0125

[25] H. S. Ahluwalia. (2003). "Solar Wind Modulation of Galactic Cosmic Rays". *Geophysical Research Letters.* **30** : 1133-1137. 10.1029/2002GL016017.

[26] A. N. I. Putri, D. Herdiwijaya, and T. Hidayat. (2024). "On the Correlation of Cosmic-Ray Intensity with Solar Activity and Interplanetary Parameters". *Solar Physics.* **299** : 12. 10.1007/s11207-023-02249-9.

[27] M. S. Callén, I. Martínez, G. Grasa, J. M. López, and R. Murillo. (2024). "Principal Component Analysis and Partial Least Squares Regression Models to Understand Sorption Enhanced Biomass Gasification". *Biomass Conversion and Biorefinery.* **14** : 2091-2111. 10.1007/s13399-022-02496-z.

[28] Q. Yan, C. Yang, and Z. Wan. (2023). "A Comparative Regression Analysis Between Principal Component and Partial Least Squares Methods for Flight Load Calculation". *Applied Sciences.* **13** : 8428. 10.3390/app13148428.

[29] A. M. Mouazen, B. Kuang, J. De Baerdemaeker, and H. Ramon. (2010). "Comparison Among Principal Component,

Partial Least Squares and Back Propagation Neural Network Analyses for Accuracy of Measurement of Selected Soil Properties with Visible and Near Infrared Spectroscopy". *Geoderma.* **158** : 23-31. 10.1016/j.geoderma.2010.03.001.

[30] D. Smart and M. Shea. (2009). "A Comparison of the Tsyganenko Model Predicted and Measured Geomagnetic Cutoff Latitudes". *Advances in Space Research.* **44** : 1107-1123. 10.1016/j.asr.2009.07.005.

[31] J. Gao, M. Korte, S. Panovska, Z. Rong, and Y. Wei. (2022). "Geomagnetic Field Shielding Over the Last One Hundred Thousand Years". *Journal of Space Weather and Space Climate.* **12** : 31. 10.1051/swsc/2022027.

[32] M. A. El-Borie. (2001). "North–South Asymmetry of Interplanetary Plasma and Solar Parameters". *Il Nuovo Cimento C.* **24** : 843-858.

[33] M. K. James, S. M. Imber, E. J. Bunce, T. K. Yeoman, M. Lockwood, M. J. Owens, and J. A. Slavin. (2017). "Interplanetary Magnetic Field Properties and Variability Near Mercury's Orbit". *Journal of Geophysical Research: Space Physics.* **122** : 7907-7924. 10.1002/2017JA024435.

[34] D. Herdiwijaya. (2019). "Distribution of Solar Energetic Particles and Magnetic Field Orientations Related to Strong Geomagnetic Storms in Solar Cycle 24". *Journal of Physics: Conference Series*. **1204** : 012121. 10.1088/1742-6596/1204/1/012121

[35] B. J. Butler, D. B. Campbell, I. de Pater, and D. E. Gary. (2004). "Solar System Science with SKA". *New Astronomy Reviews.* **48** : 1511. 10.1016/j.newar.2004.09.031.

[36] E. Kilpua, H. E. J. Koskinen, and T. I. Pulkkinen. (2017). "Coronal Mass Ejections and Their Sheath Regions in Interplanetary Space". *Living Reviews in Solar Physics.* **14** : 5. 10.1007/s41116-017-0009-6.

[37] S. Fu, X. Zhang, L. Zhao, and Y. Li. (2021). "Variations of Galactic Cosmic Rays in the Recent Solar Cycles". *The Astrophysical Journal Supplement Series.* **254** : 37-48. 10.3847/1538-4365/abf936.

[38] K. W. Chapman, S. H. Lapidus, and P. J. Chupas. (2015). "Applications of Principal Component Analysis to Pair Distribution Function Data". *Journal of Applied Crystallography.* **48** : 1619-1626. 10.1107/S1600576715016532.

[39] J. N. Miller and J. C. Miller. (2005). "Statistics and Chemometrics for Analytical Chemistry". Prentice Hall, England. 10.1002/9780470988459.ch8.

[40] T. Cserháti. (2010). "Data Evaluation in Chromatography by Principal Component Analysis". *Biomedical Chromatography.* **24** : 20-28. 10.1002/bmc.1294.

[41] A. T. Widyaninggar, K. Triyana, and A. Rohman. (2012). "Differentiation Between Porcine and Bovine Gelatin in Commercial Capsule Shells Based on Amino Acid Profile and Principal Component Analysis". *Indonesian Journal of Pharmacy.* **23** : 104-109.

[42] P. Gratier, E. Born, M. Gerin, J. Pety, V. V. Guzman, J. Orkisz, S. Bardeau, J. R. Goicoechea, F. L. Petit, H. Liszt, K. Oberg, N. Peretto, E. Roueff, A. Sievers, and P. Tremblin. (2017). "Dissecting the Molecular Structure of the Orion B Cloud: Insight from Principal Component Analysis". *Astronomy and Astrophysics.* **599** : A100. 10.1051/0004-6361/201629847.

[43] F. Murtagh and A. Heck. (1987). "Multivariate Data Analysis". Reidel Publishing Company. 10.1007/978-94-009-3789-5.

[44] R. A. Cabanac, V. de Lapparent, and P. Hickson. (2002). "Classification and Redshift Estimation by Principal Component Analysis". *Astronomy and Astrophysics.* **389** : 1090-1116. 10.1051/0004-6361:20020665.

[45] O. Okike and A. B. Collier. (2011). "A Multivariate Study of Forbush Decrease Simultaneity". *Journal of Atmospheric and Solar-Terrestrial Physics.* **73** : 796-804. 10.1016/j.jastp.2011.01.015.

[46] D. J. R. Nordemann, N. R. Rigozo, M. P. de Souza Echer, and E. Echer. (2008). "Principal Components and Iterative Regression Analysis of Geophysical Series: Application

to Sunspot Number (1750–2004)". *Computers and Geosciences.* **34** : 1443-1453. 10.1016/j.cageo.2007.09.022.

[47] R. B. Cattell. (1966). "The Scree Test for the Number of Factors". *Multivariate Behavioral Research.* **1** : 245-276. 10.1207/s15327906mbr0102_10.

[48] J. G. Luhmann, N. Gopalswamy, L. K. Jian, and N. Lugaz. (2020). "ICME Evolution in the Inner Heliosphere". *Solar Physics.* **295** (4). 10.1007/s11207-020-01624-0.

[49] E. Palmerio, C. O. Lee, I. G. Richardson, T. Nieves-Chinchilla, L. F. G. Dos Santos, J. R. Gruesbeck, N. V. Nitta, M. L. Mays, J. S. Halekas, C. Zeitlin, S. Xu, M. Holmström, Y. Futaana, T. Mulligan, B. J. Lynch, and J. G. Luhmann. (2022). "CME Evolution in the Structured Heliosphere and Effects at Earth and Mars During Solar Minimum". *Space Weather.* **20** (9). 10.1029/2022sw003215.

[50] A. Lara, N. Gopalswamy, R. A. Caballero-Lopez, S. Yashiro, H. Xie, and J. F. Valdes-Galicia. (2005). "Coronal Mass Ejections and Galactic Cosmic Ray Modulation". *The Astrophysical Journal.* **625** : 441-450. 10.1086/428565.

[51] H. V. Cane. (2000). "Coronal Mass Ejections and Forbush Decreases". *Space Science Reviews.* **93** : 55-77. 10.1023/A:1026532125747.

[52] H. Mavromichalaki, E. Paouris, and T. Karalidi. (2007). "Cosmic Ray Modulation: An Empirical Relation with Solar and Heliospheric Parameters". *Solar Physics.* **245** : 369-390. 10.1007/s11207-007-9043-1.

[53] K. Kudela, M. Storini, M. Y. Hofer, and A. Belov. (2000). "Cosmic Rays in Relation to Space Weather". *Space Science Reviews.* **93** : 153-174. 10.1023/A:1026540327564.

[54] A. Belov, L. Baisultanova, E. Eroshenko, H. Mavromichalaki, V. Yanke, V. Pchelkin, C. Plainaki, and G. Mariatos. (2005). "Magnetospheric Effects in Cosmic Rays During the Unique Magnetic Storm of November 2003". *Journal of Geophysical Research: Space Physics.* **110**. 10.1029/2005JA011067.

[55] J. T. Gosling, D. J. McComas, J. L. Phillips, and S. J. Barnes. (1991). "Geomagnetic Activity Associated with Earth Passage of Interplanetary Shock Disturbances and Coronal Mass Ejections". *Journal of Geophysical Research: Space Physics.* **96** : 7831-7839. 10.1029/91JA00316.

[56] R. Chhiber, P. Subedi, A. V. Usmanov, W. H. Matthaeus, D. Ruffolo, M. L. Goldstein, and T. N. Parashar. (2017). "Cosmic-Ray Diffusion Coefficient Throughout the Inner Heliosphere from Global Solar Wind Simulation". *The Astrophysical Journal Supplement Series.* **230** : 21. 10.3847/1538-4365/aa74d2.

[57] R. D. Strauss, M. S. Potgieter, I. Büsching, and A. Kopp. (2012). "Modelling Heliospheric Current Sheet Drift in Stochastic Cosmic Ray Transport Models". *Astrophysics and Space Science.* **339** : 223-236. 10.1007/s10509-012-1003-z.

[58] N. A. Van Bui, I. M. Martin, C. A. Vieira, Y. I. Stozhkov, and M. I. Fradkin. (1991). "Atmospheric Cosmic Rays in the South Atlantic Anomaly Region". *Il Nuovo Cimento C.* **14** : 145-151. 10.1007/BF02509394.

[59] O. Adriani, G. C. Barbarino, G. A. Bazilevskaya, R. Bellotti, M. Boezio, E. A. Bogomolov, M. Bongi, V. Bonvicini, S. Borisov, S. Bottai, A. Bruno, F. Cafagna, D. Campana, R. Carbone, P. Carlson, M. Casolino, G. Castellini, L. Consiglio, M. P. De Pascale, C. De Santis, N. De Simone, V. Di Felice, A. M. Galper, W. Gillard, L. Grishantseva, G. Jerse, A. V. Karelin, M. D. Kheymits, S. V. Koldashov, S. Y. Krutkov, A. N. Kvashnin, A. Leonov, V. Malakhov, L. Marcelli, A. G. Mayorov, W. Menn, V. V. Mikhailov, E. Mocchiutti, A. Monaco, N. Mori, N. Nikonov, G. Osteria, F. Palma, P. Papini, M. Pearce, P. Picozza, C. Pizzolotto, M. Ricci, S. B. Ricciarini, L. Rossetto, R. Sarkar, M. Simon, R. Sparvoli, P. Spillantini, Y. I. Stozhkov, A. Vacchi, E. Vannuccini, G. Vasilyev, S. A. Voronov, Y. T. Yurkin, J. Wu, G. Zampa, N. Zampa, and V. G. Zverev. (2011). "The Discovery of Geomagnetically Trapped Cosmic-Ray Antiprotons". *The Astrophysical Journal Letters.* **737** : L29. 10.1088/2041-8205/737/2/L29.